Transport of Single-Layered Graphene Oxide Nanosheets through Quartz and Iron Oxide–Coated Sand Columns

Thomas A. Duster[1]; Chongzheng Na[2]; Diogo Bolster[3]; and Jeremy B. Fein[4]

Abstract: Single-layered graphene oxide (SLGO) nanosheets are distinguished from other colloids by their extreme anisotropy, which likely exerts a strong control on their transport behavior. Hence, this study investigates the influence of both environmentally relevant pH and ionic strength on the transport of SLGO nanosheets through saturated quartz or iron oxide–coated sands. Both the nanosheets and quartz sands are negatively charged throughout the experimental conditions, resulting in very little nanosheet deposition onto the quartz sands. However, increasing ionic strength and decreasing pH did cause measurable increases in nanosheet deposition, likely due to decreases in the magnitude of negative charges near the respective surfaces. Conversely, nanosheets and iron oxide–coated sands are oppositely charged throughout the experimental conditions, resulting in significant nanosheet deposition onto the iron oxide–coated sands. These trends suggest that nanosheet deposition is largely controlled by electrostatic forces, although the deposition rate of the high ionic strength iron oxide–coated sand treatment could not be explained by electrostatic interactions alone and instead may be influenced by nanosheet aggregation. Collectively, these measurements enable prediction of SLGO transport throughout a range of realistic environmental and geologic conditions. **DOI: 10.1061/(ASCE)EE.1943-7870.0001156.**

Author keywords: Single-layered graphene oxide (SLGO); Deposition rate; Transport; Quartz; Iron oxide.

Introduction

Natural flake graphite is comprised of atomically thin graphene laminations (Novoselov et al. 2004), which can be oxidized and exfoliated after exposure to a strong mix of acids, chemical oxidants, and ultrasonication (Hummers and Offeman 1958; Stankovich et al. 2007). When completely exfoliated, the resulting nanosheets, called single-layered graphene oxide (SLGO), exhibit a platelike morphology and a high degree of anisotropy, measuring ~1 nanometer (nm) in thickness and up to several micrometers in diameter (Chen et al. 2009; Gao et al. 2009; Park and Ruoff 2009; Zhang et al. 2010). While the chemical structure of SLGO nanosheets may vary with differences in fabrication details (Szabo et al. 2006a; Dreyer et al. 2010), it is generally agreed that the oxidation of the graphene laminations serves to intercalate and decorate the regular lattice of six-membered carbon rings with various oxygen-containing functional groups. These groups may include covalently bonded epoxide, ketone, and hydroxyl groups on the basal planes, and carboxylic, lactol, and phenolic groups at the edges (Lerf et al. 1998; Szabo et al. 2006a; Gao et al. 2009; Lee et al. 2010), which when considered collectively, populate the surface at an average proton active site density of up to ~1 site nm^{-2} across a nanosheet surface area exceeding 1,800 $m^2\ g^{-1}$ (Szabo et al. 2006b; Duster et al. 2015). Hence, SLGO nanosheets are characterized by an extremely large and reactive surface area for interactions with mobile-phase and stationary-phase environmental constituents.

In fact, systems containing graphene oxide at varying degrees of exfoliation exhibit extraordinarily high sorption capacities for a wide variety of compounds, including toxic metals (Zhao et al. 2011a, c, 2012; Sitko et al. 2013; Duster et al. 2015) and complex organic pollutants (Hartono et al. 2009; Ion et al. 2011; Zhang et al. 2011; Gao et al. 2012), making them ideally suited for use in both in situ and ex situ water, groundwater, and soil remediation applications (Romanchuk et al. 2013; Wang et al. 2013). However, in order to deploy SLGO nanosheets in polluted environments and/or engineered remediation systems, one must first understand the factors that control their mobility through a variety of porous media. While the literature is replete with studies related to the transport of various colloidal materials (Johnson et al. 1996; Johnson and Logan 1996; Ryan and Elimelech 1996; Kretzchmar et al. 1999; Bradford et al. 2002, 2003; Sen and Khilar 2006; Xu et al. 2006), the extreme anisotropy, distinctive dimensions, and large reactive surface area distinguishes SLGO nanosheets from these other well-studied colloids. For example, relative to SLGO nanosheets, some clays exhibit a similar platelike morphology (Tournassat et al. 2003), but dramatically lower surface areas (< 300 $m^2\ g^{-1}$) for interactions with stationary collectors (Dogan et al. 2006, 2007). The chemical composition and effective surface areas of carbon nanotubes (up to 1,300 $m^2\ g^{-1}$ depending on the number of walls; Peigney et al. 2001) are comparable to that of SLGO nanosheets, but their long and slender aspect strongly influences transport behaviors (Jaisi et al. 2008; Jaisi and Elimelech 2009). As a result, it would be exceedingly difficult to confidently apply the results of this body of literature to predict the transport behaviors of SLGO nanosheets in the environment.

[1]Geochemist, Applied Chemicals and Materials Division, Material Measurement Laboratory, National Institute of Standards and Technology, 325 Broadway, Boulder, CO 80305; formerly, Ph.D. Student, Dept. of Civil and Environmental Engineering and Earth Sciences, Univ. of Notre Dame, 156 Fitzpatrick Hall, Notre Dame, IN 46556 (corresponding author). E-mail: thomas.duster@nist.gov

[2]Assistant Professor, Dept. of Civil and Environmental Engineering and Earth Sciences, Univ. of Notre Dame, 156 Fitzpatrick Hall, Notre Dame, IN 46556.

[3]Assistant Professor, Dept. of Civil and Environmental Engineering and Earth Sciences, Univ. of Notre Dame, 156 Fitzpatrick Hall, Notre Dame, IN 46556.

[4]Professor, Dept. of Civil and Environmental Engineering and Earth Sciences, Univ. of Notre Dame, 156 Fitzpatrick Hall, Notre Dame, IN 46556.

Note. This manuscript was submitted on November 20, 2015; approved on May 24, 2016; published online on August 2, 2016. Discussion period open until January 2, 2017; separate discussions must be submitted for individual papers. This paper is part of the ***Journal of Environmental Engineering***, © ASCE, ISSN 0733-9372.

To date, few existing studies have specifically investigated the transport of SLGO nanosheets through saturated porous media. Of the studies that do exist, most focus primarily on the influence of ionic strength on nanosheet transport behaviors through quartz sand, while leaving pH either uncontrolled/unreported (Liu et al. 2013a; Qi et al. 2014a) or fixed near pH 5 (Qi et al. 2014b), pH 5.4 (Lanphere et al. 2013), or pH 6 (Feriancikova and Xu 2012). Additionally, Liu et al. (2013b) investigated the transport of carboxyl-functionalized graphene in quartz and metal oxyhydroxide–coated sands at pH 5.6 and 8.3 but did not control the ionic strengths of the suspending solutions, and two reports from Qi et al. (2014a, b) investigated the influence of pH on SLGO transport but at a fixed ionic strength. While these studies attempted to isolate the influence of individual solution properties and/or surface chemistries on SLGO transport parameters, each fails to consider the combined interplay that pH, ionic strength, and collector surface mineralogy can have on nanosheet mobility. Hence, additional studies are required to accurately predict the fate and transport of SLGO nanosheets in realistic geologic systems that vary within a broad range of environmental conditions.

This study investigates the influence of both environmentally-relevant pH (5.6–8.3) and ionic strength (10 and 50 mM), as well as sand grain surface coatings (quartz and iron oxide), on the transport of SLGO nanosheets through saturated porous media. The results indicate that the relative electrochemical properties of the nanosheet and sand surfaces, as determined by both the pH and ionic strength of a given treatment, are the primary factors that control the mobility of SLGO through saturated porous media. Aggregation at high ionic strength may also influence SLGO nanosheet transport.

Experimental Procedures

SLGO Nanosheet and Porous Media Preparation/ Characterization

A complete protocol for the synthesis of SLGO nanosheets (Hummers and Offeman 1958) and specific details regarding the nanosheet characterization methods are provided in the Supplemental Data. Briefly, the physical properties of the SLGO nanosheets utilized in subsequent transport experiments were characterized using atomic force microscopy (AFM; XE-70, Park Systems, Santa Clara, California), which illustrated a heterogeneous nanosheet length/width distribution ranging from several hundred nanometers to approximately 1.5μm in diameter [Figs. 1(a and b)]. SLGO heights generally ranged between 1.0 and 1.5 nm [Fig. 1(c)], which is indicative of single-layered nanosheets (Park and Ruoff 2009; Zhang et al. 2010). In addition, UV-visible (UV-vis) spectrophotometry (Figs. S1 and S2), dynamic light scattering (DLS), and electrophoretic mobility (EPM) measurements were obtained from nanosheet suspensions throughout a range of experimentally relevant pH and ionic strength conditions. Similar to clay platelets (Lagaly 2006), the nonspherical shape of SLGO nanosheets precludes the use of EPM measurements to calculate ζ-potential values directly, making the EPM values a preferred proxy for near-surface charge. Details and results of these studies are described as needed throughout the main text.

A thorough description related to the preparation, washing, and characterization of the quartz sand and iron oxide–coated sand collectors used in the column experiments is provided in the Supplemental Data. Briefly, acid-washed quartz sand (Accusand, Unimin Corporation, LeSueur, Minnesota) was utilized as the solid-phase stationary medium for all uncoated sand column experiments and as the base grain for all iron oxide–coated sand column experiments. Supplier specifications indicate a grain size range of 0.29–0.44 mm. An iron oxide coating was precipitated onto the suspended quartz sand base during titration of a 0.05M $Fe(NO3)_3 \cdot 9H_2O$ (Sigma-Aldrich; ACS grade) solution (Ams et al. 2004). The authors evaluated the morphological and chemical characteristics of individual grains from the quartz and iron oxide–coated sands via scanning electron microscopy (SEM; Leo-EVO 50, Carl Zeiss, Oberkochen, Germany) and energy dispersive X-ray spectroscopy (EDX; Oxford Instruments, Abingdon, United Kingdom). In addition, some surface-associated colloidal material was collected from the quartz and iron oxide–coated sand grains via probe sonication and vigorous vortexing, respectively, and subjected to an EPM titration throughout the experimental range of ionic strength and pH. The material removed completely encapsulated the underlying base-mineral grain (Fig. S3) and is therefore representative of the outer surface of the collector that interacts with the SLGO nanosheets. Hence, EPM measurements of the surface-associated colloidal material can be viewed as a proportional surrogate for the near-surface charge (i.e., ζ-potential) of an individual grain (Jaisi et al. 2008; Smith et al. 2008).

Column Transport Studies

All SLGO transport studies were conducted using borosilicate glass columns (FlexColumn, Kimble-Kontes Scientific, Vineland, New Jersey) measuring 10.0 cm long by 1.0 cm in diameter. For both quartz sand and iron oxide–coated sand experiments, 8.0 g of fresh material was rinsed twice with ionic strength buffer and ultrapure water [$R > 18$ MΩ cm, total organic carbon (TOC) < 2 μgCL^{-1}]

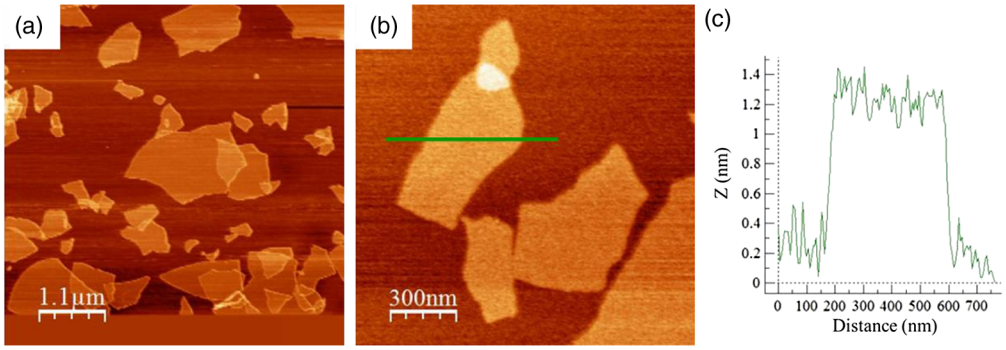

Fig. 1. Two characteristic noncontact AFM images of SLGO nanosheets deposited on freshly-cleaved mica; the scale changes between images (a) and (b); panel (c) illustrates the height or z-dimension profile from the cross section depicted on panel (b); collectively, these panels indicate the dominant presence of SLGO nanosheets that have been completely exfoliated [(a) and (b) republished from Duster et al. 2015, with permission from Elsevier]

to remove loosely associated colloidal material and then slowly added to a column prefilled with ultrapure water. The sand was settled by vigorously vibrating and tapping the filled columns. The average calculated porosity for each experimental system was 0.34, which is within the range of typical porosities for natural sand dominated systems. The influent flow rate for each column transport study was 1 mL min^{-1} driven by a peristaltic pump, which resulted in an approach (superficial) velocity of 0.0212 cm s^{-1} (details provided in the Supplemental Data).

Prior to the start of an experiment, each packed column was initially rinsed with 12.5 pore volumes of ultrapure water (which is not accounted for on subsequent figures). Columns were then conditioned to the target pH and ionic strength for each respective experimental treatment. In both conditioning solutions and SLGO-containing suspensions, an ionic strength of either 10 or 50 mM was achieved using appropriate additions of $NaClO_4 \cdot H_2O$ (Fisher Scientific, Waltham, Massachusetts; ACS grade), while influent pH was adjusted to and maintained at (± 0.1 s.u.) the environmentally relevant values of pH 5.6, 7.0, and 8.3 using repeated additions of 0.01 to 0.1 M NaOH, as needed. The authors opted against the use of chemical buffers to maintain pH in the experimental systems (for reasons outlined in the Supplemental Data), and instead regularly monitored both the influent and effluent pH values, as reported in subsequent sections, in order to accurately represent the gradient of pH conditions existing within a given column system. The largest change in precolumn and postcolumn pH occurred in high pH systems exposed to the iron oxide–coated sands.

After 12.5 pore volumes of conditioning, a manual valve system served to seamlessly switch the column flow to a solution containing 25 mg SLGO L^{-1} suspended in the identical background electrolyte used to condition the column. The SLGO suspension flowed continuously through the column for 50 pore volumes, at which time the flow was again switched back to the SLGO-free background electrolyte solution for an additional 12.5 pore volumes. To measure the SLGO nanosheet concentration during breakthrough, the absorbance of the column effluent was monitored at $\lambda = 230$ nm at 6 s intervals (C_t) using a spectrophotometer (Cary 100, Agilent Technologies, Santa Clara, California) equipped with a 1-cm flow-through quartz cuvette. All suspensions of SLGO nanosheets exhibited a peak UV-vis absorbance near $\lambda = 230$ nm. Absorbance at this wavelength is linearly correlated with SLGO concentration (Fig. S2), making all decreases in absorbance attributable to changes in SLGO nanosheet concentrations due to deposition in the column (Fig. S1). Hence, normalizing the C_t values to the initial absorbance of the influent SLGO suspension (C_0) results in breakthrough curves that relate the normalized concentration ratio (C_t/C_0) to the numbers of pore volumes that have passed through the column. Column transport studies for each pH and ionic strength treatment condition were conducted at least in duplicate. Replicate runs largely overlap, and thus, an average breakthrough curve is presented for each treatment in subsequent figures and analyses, with the actual replicate data presented in the Supplemental Data. In addition to these experiments, in order to account for the internal volume of the overall flow system and specific column dispersion characteristics, the breakthrough of a 5 mM NaBr conservative tracer solution ($\lambda = 218$ nm) was separately monitored using the identical flow-through UV-vis spectrophotometer setup that was previously described (Fig. S4).

Quantitative Characterization of Transport Parameters

When colloid release rates are small (e.g., irreversible sorption), the transport of colloidal particles through porous media under steady-state saturated-flow conditions is traditionally described using a modified mobile-immobile advection-dispersion equation (Kretzschmar et al. 1997) as follows:

$$\frac{\partial C}{\partial t} = D_p \frac{\partial^2 C}{\partial x^2} - v_p \frac{\partial C}{\partial x} - k_d C \tag{1}$$

where C = concentration of suspended particles; D_p = dispersion coefficient; v_p = average linear water velocity; x = travel distance in the direction of water flow; and k_d = colloid deposition rate coefficient. The first two terms on the right side of Eq. (1) represent dispersive and advective transport, respectively. For systems where dispersive transport is negligible, relative to advective transport, Eq. (1) reduces to the following estimate for the colloid deposition rate coefficient, k_d:

$$k_d = -\frac{U}{fL} \ln\left(\frac{C}{C_0}\right) \tag{2}$$

where f = packed bed porosity; U = approach velocity; L = length of the packed bed; and C/C_0 = breakthrough concentration or the fraction of colloids observed in the column effluent after the breakthrough curve reaches a plateau (Kretzschmar et al. 1997, 1999; the definition of C/C_0 is further elaborated in subsequent sections). The first term in Eq. (2) equates to the average travel time of colloidal particles through the column, making k_d a time-averaged and distance-averaged parameter. In addition, for clarity and consistency with filtration theory (Yao et al. 1971; Tufenkji and Elimelech 2004), the authors note that the deposition rate coefficient is proportional to the single collector efficiency (η) using the following relationship:

$$k_d = \frac{3(1-f)U}{2f d_c} \eta \tag{3}$$

where d_c = grain diameter for the collector grains.

The k_d values for each experimental treatment were calculated and then compared to the k_d value from an electrostatically favorable deposition condition to establish an attachment efficiency (α). As will be seen in subsequent sections, SLGO nanosheets are negatively charged throughout the range of experimental conditions in this study, while the iron oxide–coated sand grains exhibit a positive charge at the pH values studied, particularly at the lowest pH investigated. Hence, the k_d value from the 50 mM ionic strength, low pH, iron oxide–coated sand treatment was designated as the $k_{d,fav}$, and the attachment efficiency (α) was calculated as

$$\alpha = \frac{k_d}{k_{d,fav}} \tag{4}$$

The following analysis then uses k_d and α values for each experimental treatment as the metrics by which to compare and evaluate the transport of SLGO nanosheets through systems that vary in pH, ionic strength, and collector grain coatings.

Results and Discussion

Electrochemical Characterization of SLGO and Collector Grains

Fig. 2 illustrates the EPM measurements for SLGO nanosheets, quartz sand grains, and iron oxide–coated sand grains exposed to the pH range (~5.5 to ~8.5) and ionic strengths (10 and 50 mM) of interest. Both the SLGO nanosheets and quartz sand colloids are negatively charged throughout this range of pH and ionic strength. EPM values ranged from -1.5 to -3.3 μm cm V^{-1} s^{-1} for quartz

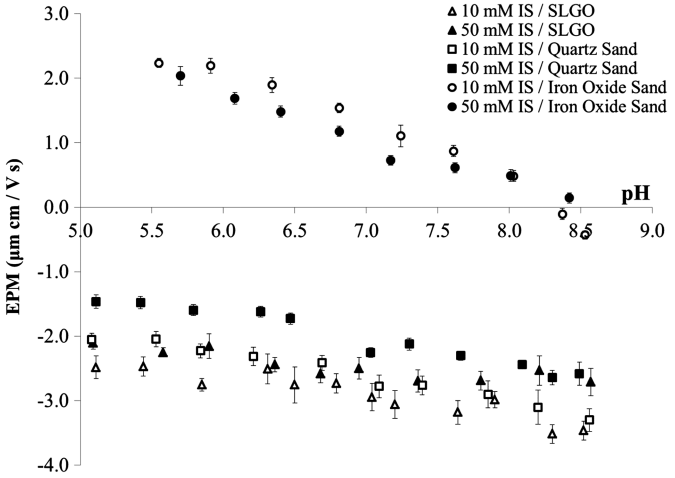

Fig. 2. Electrophoretic mobility (EPM) measurements titrated against pH for SLGO nanosheets, quartz sand grains (surface-associated colloidal material), and iron oxide–coated sand grains (surface-associated colloidal material) suspended in an electrolyte solution exhibiting an ionic strength of 10 or 50 mM; error bars represent one standard deviation, but may be obscured by the point when sufficiently small

sand colloids and −2.0 to −3.5 μm cm V^{-1} s^{-1} for SLGO nanosheets, with the more negative EPM values occurring in high pH and low ionic strength systems. Quartz sand surfaces display proton active hydroxyl functional groups at their edges (Pagnanelli et al. 2006), while SLGO nanosheet surfaces exhibit several ionizable functional groups (Lerf et al. 1998; Szabo et al. 2006a; Gao et al. 2009), including carboxyl and hydroxyl groups with pK_a values that range between 4.3 and 10.0 (Konkena and Vasudevan 2012; Duster et al. 2015). Hence, increasing pH favors the deprotonation of these surface-associated functional groups, thereby leading to more negatively charged surfaces at high pH. Increases in ionic strength result in a concentration-dependent buildup of counter ions from the background electrolyte near the particle surfaces and a consequent compression of the electric double layer. This phenomenon effectively screens some of the surface charge, thereby leading to a diminished negative charge near the particle surface in high ionic strength conditions.

Iron oxide–coated sand colloids are positively charged at all but the highest pH values evaluated and, relative to quartz sand colloids, are not as sensitive to changes in ionic strength. For example, the iron oxide–coated sand colloids exposed to electrolyte solutions of 10 and 50 mM ionic strength exhibited an EPM of greater than +2.0 μm cm V^{-1} s^{-1} between pH 5.6 and 5.7, respectively, with each reaching their point-of-zero-charge (pH_{zpc}) near or above pH 8.3. Similar to the quartz sand, increases in pH lead to deprotonation of the hydroxyl edge site functional groups at the iron oxide surface (Davis and Leckie 1978), thereby resulting in fewer positively charged sites.

Column Transport Studies

This study reports on a series of column transport experiments that investigated the mobility of SLGO nanosheets through porous quartz and iron oxide–coated sand media in systems exhibiting environmentally relevant pH and ionic strength conditions. The results of these studies are depicted in Fig. 3. Near the end of each study where flow to the column is switched from the SLGO suspension to a SLGO-free suspension exhibiting the same pH and ionic strength conditions (62.5 pore volumes), a precipitous decline in effluent SLGO concentrations with little tailing is observed. This observation supports an assumption of irreversible sorption of SLGO nanosheets to the collector grains throughout all experimental conditions, thereby validating the use of Eq. (2) to calculate the deposition rate coefficient, which is used as a primary metric in this study.

For most experimental treatments, the normalized SLGO effluent concentrations illustrated by these breakthrough curves never plateau at a steady-state value following the initial dispersive region of the curve, but rather slowly increase with time throughout the experiment. The shapes of these breakthrough curves are characteristic of systems where the initial retention of SLGO nanosheets within the column serves to block subsequent nanosheets from interacting with the collector (Ryan and Elimelech 1996). The constant flow of SLGO nanosheets being delivered to the columns likely resulted in the blocking of many available sorption sites and contributed to the eluting of greater numbers of nanosheets with increasing time over the duration of the experiments. The magnitude of this effect on deposition rates is not necessarily proportional to the number of sites blocked, as each adsorbed nanosheet will effectively extend the influence of the collector (Song and Elimelech 1993), based on its size, shape, and electric double-layer properties.

This phenomenon requires the designation of a "clean-bed" breakthrough concentration for the calculation of an "initial" deposition rate, k_d (Kretzschmar et al. 1997, 1999). In order to apply this modeling approach, the C/C_0 term of Eq. (2) is defined as the normalized clean-bed breakthrough concentration at a point where attachment sites are not limiting. While previous studies using an identical analytical approach identify the clean-bed breakthrough concentration at between 1.8 and 2.0 pore volumes beyond sample introduction (Redman et al. 2004; Jaisi et al. 2008), the definition used herein requires consideration of a slightly larger internal system volume (e.g., a flow-through cuvette with a larger volume). Hence, for the determination of k_d, the normalized clean-bed breakthrough concentrations is obtained at 5.5 pore volumes after beginning the constant injection of the SLGO suspension to the column, which equates to 18 total pore volumes from the start of the experiments (when considering the 12.5 pore volumes of conditioning), as indicated in Fig. 3. As in previous studies, this clean-bed breakthrough concentration equates to the point on a breakthrough curve where the C_t/C_0 value of the conservative NaBr tracer exceeds 0.99, indicating that sufficient time has passed to allow for the advection and dispersion of the mobile target. The calculated k_d values are presented in Fig. 4 against the pH observed in the effluent of the treatment columns.

SLGO nanosheets in quartz sand treatments at relatively high ionic strength were deposited to a much greater extent than those at low ionic strength. A similar trend has been observed in previous studies of SLGO transport in ionic strength treatments ranging from 1 to 100 mM (Feriancikova and Xu 2012; Liu et al. 2013a; Lanphere et al. 2013; Qi et al. 2014a, b). However, unlike several previous studies that either did not control pH (Liu et al. 2013a) or held pH constant throughout the study (Feriancikova and Xu 2012; Lanphere et al. 2013), this study indicates that within a given ionic strength treatment, pH also plays a pronounced role in determining the mobility of nanosheets through porous media. For example, k_d values for the high pH, middle pH, and low pH treatments at high ionic strength were 2.1×10^{-3}, 2.8×10^{-3}, and 4.3×10^{-3} s^{-1}, respectively, with attachment efficiencies of up to 90% at the lowest pH evaluated (Fig. 4). As indicated by the similarity between the SLGO and NaBr breakthrough curves in the low ionic strength systems containing quartz sand [Fig. 3(a)], relatively few SLGO nanosheets were deposited under these treatment conditions, but

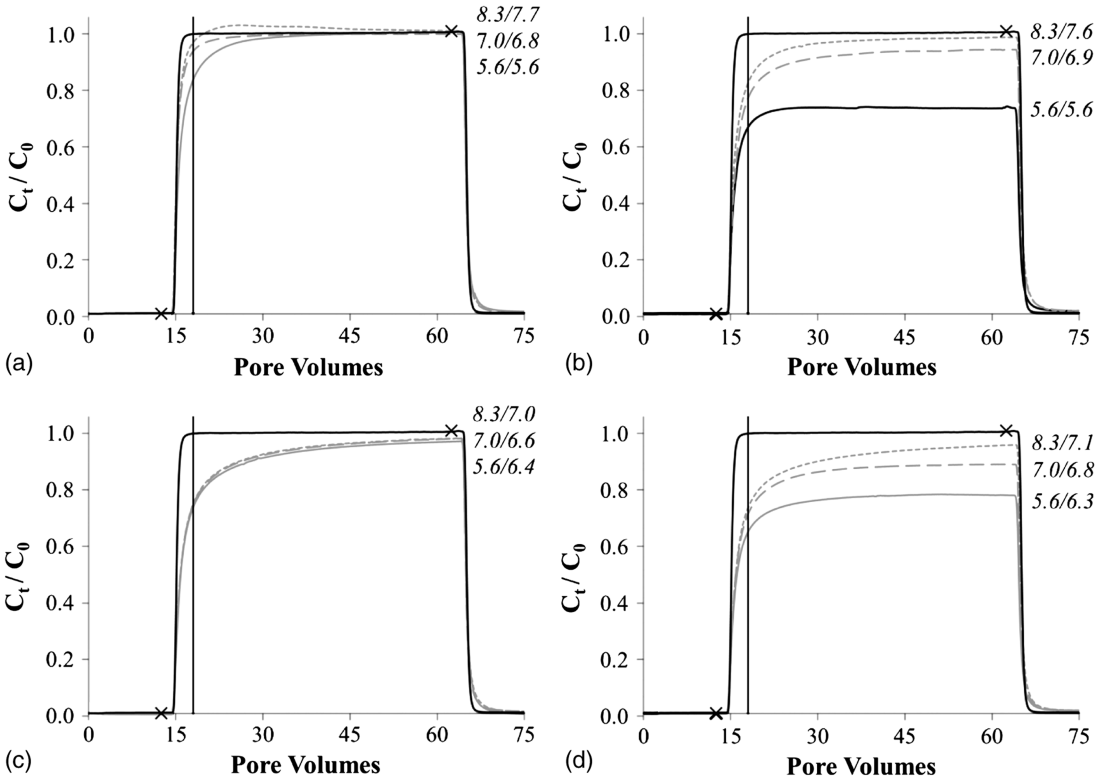

Fig. 3. Breakthrough curves for quartz sand columns: (a) 10 mM; (b) 50 mM ionic strength; and iron oxide–coated sand columns: (c) 10 mM; (d) 50 mM ionic strength; dotted, dashed, and solid gray curves represent the average breakthrough for treatments with an influent pH of 8.3, 7.0, and 5.6, respectively; the black curve is the average breakthrough for the NaBr tracer (see Supplemental Data); pH values to the right of the breakthrough curves follow the convention: *Influent pH/Effluent pH*; continuous flow of an SLGO suspension occurred between 12.5 and 62.5 pore volumes (marked with black × s), with a pH-matched SLGO-free ionic strength buffer solution flowing through the column at all other times depicted in the figure; not shown on these figures is an initial column rinse with ultrapure water, which preceded each transport experiment; a horizontal black line at 18 pore volumes indicates where the clean-bed breakthrough concentration is measured for Eq. (2); additional details regarding this figure, including a discussion of any C_t/C_0 values greater than 1.0, can be found in the Supplemental Data

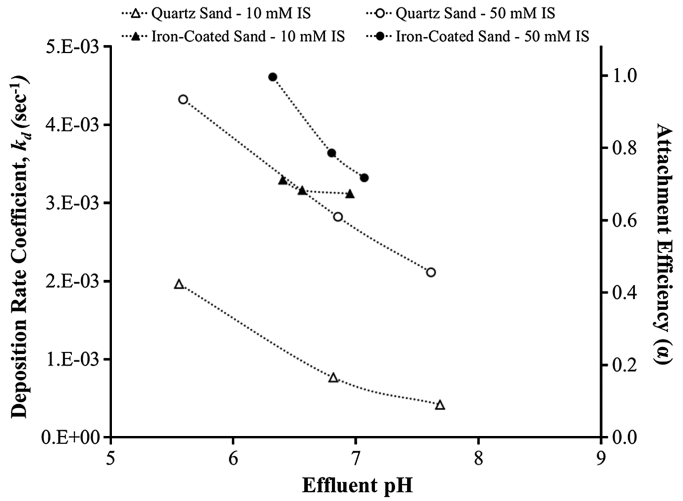

Fig. 4. Initial deposition rate coefficients (k_d) and attachment efficiencies (α) for SLGO nanosheets transported through columns packed with quartz sand and iron oxide–coated sand in the pH and ionic strength conditions noted; all k_d values were calculated from the breakthrough concentrations presented in Fig. 3 and are plotted against the average effluent pH values recorded for replicates from each treatment

the SLGO transport behaviors were still measurably influenced by pH. In the low ionic strength quartz systems, the k_d values were calculated as 0.4×10^{-3}, 0.8×10^{-3}, and 2.0×10^{-3} s^{-1} for the high pH, middle pH, and low pH systems, respectively. Collectively, these data illustrate the importance of considering both ionic strength and pH when evaluating the transport of SLGO nanosheets through porous media.

Due to the strong influence of surface mineralogy on the pH of the unbuffered SLGO nanosheet suspensions passing through columns packed with iron oxide–coated sands (see details provided in the Supplemental Data), this study was only able to evaluate the transport behavior of SLGO nanosheets through a restricted pH range (effluent pH values of 6.4–7.0 and 6.3–7.1 for the 10 and 50 mM ionic strength treatments, respectively). Breakthrough curves for each of the low ionic strength iron oxide–coated sand treatments approximately overlapped [Fig. 3(c)], translating to a small range of k_d values of between 3.1×10^{-3} and 3.3×10^{-3} s^{-1}, which is likely due in part to the limited effluent pH range evaluated. Relative to the low ionic strength treatments, SLGO nanosheets in the high ionic strength iron oxide–coated sand treatments were deposited to a much greater extent. In fact, these treatments resulted in the highest k_d values for a given effluent pH across all experimental treatments (3.3×10^{-3}, 3.7×10^{-3}, and 4.6×10^{-3} s^{-1} for the effluent pH values of 7.1, 6.8, and 6.3, respectively). Even within the restricted pH range, these data

also illustrate that increases in pH resulted in increased breakthrough concentrations and decreased deposition rates. Liu et al. (2013b) also observed decreasing deposition of carboxyl-functionalized graphene sheets with increasing pH (at an unreported ionic strength) in natural sand that contained metal oxyhydroxide surface coatings.

Physical and Electrochemical Mechanisms Associated with Observed Transport Behaviors

Figs. 3 and 4 illustrate several important trends in the transport behavior of SLGO nanosheets with respect to pH, ionic strength, and mineral coating. First, the larger deposition rates for SLGO nanosheets in columns containing quartz sand at high ionic strength, relative to those in low ionic strength treatments, is in qualitative agreement with the interactions predicted by Derjanuin-Landau-Verwey-Overbeek (DLVO) theory. The increase in ionic strength results in an increase in the concentration of counter-ions at the surface, a consequent compression of the electric double layer for both the SLGO nanosheets and quartz sand collector, and a reduction in the repulsive energy barrier that would otherwise limit nanosheet deposition. In addition, systems at relatively low pH are characterized by higher deposition rates because more surface-associated functional groups on the nanosheet and quartz sand collector surfaces are protonated, causing each surface to be less negatively charged, thereby reducing repulsive forces. Evidence for these trends is also illustrated by the EPM values depicted in Fig. 2, which indicate that both the SLGO nanosheets and quartz sand collector are more negatively charged at high pH and low ionic strength, which favors lower k_d values.

The transport behavior of SLGO nanosheets in iron oxide–coated sand columns at low ionic strength can also be explained by the relative electrostatic properties of the nanosheets and collector grains. In this case, the iron oxide–coated sand is positively charged throughout the effluent pH range (6.4–7.0), which favors significant deposition of the negatively charged SLGO nanosheets. Indeed, over the corresponding pH range, k_d values for the low ionic strength iron oxide–coated sand treatment are over four times higher than those of the low ionic strength quartz sand treatments. Without electrostatic repulsion to overcome, pH exerts only a minor influence on deposition in these systems, as the surfaces remain oppositely charged throughout the pH range evaluated. In addition, Fig. 2 indicates that the relatively small decrease in the positive charge associated with the iron oxide coating resulting from increases in pH are approximately compensated by the increasingly negative charge on the SLGO nanosheets with increasing pH.

Unlike the experimental treatments discussed earlier, the transport behavior of the high ionic strength iron oxide–coated sand treatments cannot be explained by electrochemical interactions alone. Oppositely charged surfaces typically respond to increases in ionic strength by decreasing their interaction because their respective surface charges are effectively shielded by the presence of increasing concentrations of counter-ions. An alternative perspective on this phenomenon would suggest that the electric double layer of a surface in a low ionic strength system is thicker and extends to a greater distance into the surrounding solution, increasing the likelihood of attracting an oppositely charged particle. However, in the systems containing iron oxide–coated sands, an increase in ionic strength from 10 to 50 mM increases the interaction between the oppositely charged SLGO nanosheets and iron-oxide sand collector, leading to an increase in deposition rates (Fig. 4). The increase in deposition with increasing ionic strength occurs despite evidence for small decreases in the magnitudes of positive and negative charge for the collector and SLGO nanosheets, respectively, relative to the low ionic strength treatments, as depicted in Fig. 2.

The unanticipated behavior observed in the 50 mM ionic strength iron oxide–coated sand treatment may be explained by changes in the aggregation state of the SLGO nanosheets in the feed stock solution prior to being distributed to the packed columns. For the same reason that SLGO–quartz sand interactions increase with increasing ionic strength, compression of the electric double layer could also induce nanosheet–nanosheet aggregation. Aggregation could result in enhanced deposition of SLGO nanosheets in the 50 mM ionic strength treatments in two ways. Firstly, in systems containing aggregated nanosheets, each successful nanosheet-collector attachment would remove a greater number of individual nanosheets from the solution, relative to unaggregated systems. Secondly, depending on their size, nanosheet aggregates would likely be more prone to physical filtration mechanisms, whereby the larger particles become lodged in confined pore spaces. In the experimental systems associated with this study, the ratio between the largest axial nanosheet dimension and the smallest possible collector grain (i.e., $\sim 1.5/290$ μm$=0.005$) is approximately equivalent to reported thresholds for straining [e.g., $d_p/d_g = 0.002$ (Bradford et al. 2003) or 0.008 (Xu et al. 2006)], meaning that small changes in the physical dimensions of the SLGO nanosheets may have significant implications for their straining potential.

Results from the DLS study (Table 1) provide evidence that SLGO nanosheets may aggregate in response to the environmental conditions present in some experimental treatments. For example, at pH 5.6 and 7.0 (values that approximately bracket the effluent pH range in the iron oxide–bearing systems), average particle diameter measurements significantly increase ($p < 0.05$) as ionic strength changes from 10 to 50 mM. However, DLS-measured particle diameters are derived by assuming a spherical particle shape, and it must be emphasized that it is currently unknown whether the magnitude of change observed in these measurements of the highly anisotropic SLGO particles corresponds to relevant changes in nanosheet aggregation states. Nevertheless, previous SLGO transport studies have also provided evidence for aggregation in their highest ionic strength treatments above ~30 mM (Liu et al. 2013a; Lanphere et al. 2013). Chowdhury et al. (2013) determined that the critical coagulation concentration of SLGO nanosheets is approximately 44 mM NaCl at pH 5.5, but observed no aggregation of SLGO nanosheets at NaCl concentrations lower than 20 mM. While Chowdhury et al. (2013) only evaluated nanosheet suspension stability at pH 5.5, it is anticipated that the extent of aggregation in a solution at constant ionic strength would decrease with increasing pH as nanosheets become more negatively charged and repulsive (Fig. 2), thereby reducing nanosheet–nanosheet interactions. The average diameters observed in the DLS data follow

Table 1. DLS-Calculated Hydrodynamic Diameters for SLGO Nanosheets Exposed to Various Environmental Conditions

Ionic strength (mM)	pH (s.u.)	Average diameter (nm)	Standard deviation (nm)
10	5.6	1,186	38
10	7.0	1,175	44
10	8.3	1,129	42
50	5.6	1,271	57
50	7.0	1,232	33
50	8.3	1,144	46

Note: $n = 6$ measurements.

this expected trend. Hence, the expected impact of aggregation on SLGO deposition rates would also decrease with increasing pH, as observed in the high ionic strength iron oxide–coated sand systems (Fig. 4). Although the transport behavior in high ionic strength treatments containing quartz sand collectors can be explained by electrochemical interactions alone as previously discussed, the aggregation of SLGO nanosheets may influence deposition in these systems as well.

It is important to point out that the authors saw no impact of ionic strength or pH on the initial UV-vis absorbance spectra of the precolumn SLGO nanosheet suspensions utilized for the transport studies. Hence, nanosheets aggregating in response to increases in ionic strength did not compromise the measurement of SLGO nanosheet concentrations in the column effluents. However, because the low pH, high ionic strength iron oxide–coated sand treatment does provide the $k_{d,fav}$ parameter for the calculation of attachment efficiencies [Eq. (4) and Fig. 4], the presence of physical filtration due to aggregation in this system could influence all associated α values. The calculated k_d value for each experimental treatment is based on discrete measurements of SLGO nanosheet transport and not subject to the same analytical limitation as the α values, and may therefore be a preferable metric for describing SLGO nanosheet mobility in porous media.

Potential Influence of Shape in Graphitic Material Transport

Previous research using a similar methodology and quartz sand collectors found k_d values that are approximately 10 times higher for carboxyl-functionalized single-walled carbon nanotubes (Jaisi et al. 2008) and three to four times lower for fullerenes (Tong et al. 2010) in 10 mM ionic strength systems at pH values of 6.8–7.0, relative to the corresponding measurements reported herein. While difficult to compare directly, the EPM values for each of these graphitic materials indicates approximately similar negative near surface charges. Therefore, the authors propose that differences in shape between these graphitic materials may exert a stronger control than electrostatic forces alone on their transport behaviors through porous media. SLGO nanosheets are distinguished from fullerenes and carbon nanotubes by their platelike morphology, distinctive dimensions, and extreme anisotropy, and these distinctions do appear to follow the trends in k_d values described earlier. For example, relative to SLGO nanosheets, carbon nanotubes are likely deposited to a much greater extent due to their very long and/or bundled morphologies that could promote very high degrees of physical straining (Jaisi et al. 2008). Conversely, fullerenes are likely deposited to a much smaller extent than SLGO nanosheets due to their spherical shape.

This hypothesis is largely supported by the limited data in the literature regarding the influence of colloid shape on transport behaviors. For example, in columns packed with quartz sand, rod-shaped bacteria generally elute more slowly than spherical bacteria (Weiss et al. 1995). In addition, retention rates for polystyrene latex microparticles (~1 μm diameter) exhibiting identical near-surface charges increase with increasing aspect ratio (Salerno et al. 2006), although the role of straining in these systems is unclear and contradictory data do exist (Seymour et al. 2013). Internally consistent investigations are needed to validate the proposed relationship between deposition rates for SLGO nanosheets, fullerenes, and carbon nanotubes and the influence of SLGO dimension and anisotropy on nanosheet transport.

Environmental Implications

Initial deposition rate coefficients calculated from particle breakthrough curves demonstrated that SLGO nanosheet mobility in each mineral-bearing system decreased with increasing ionic strength and with decreasing pH. In addition, SLGO nanosheet transport was limited in columns packed with iron-coated sand, relative to those packed with quartz sand. Because the porous sand systems used in this study are relatively homogenous when compared to real environmental systems with respect to collector grain sizes, pore geometries, and soil mineralogy, the deposition rates presented herein likely overestimate the expected mobility of SLGO nanosheets in actual subsurface environments. Still, understanding transport behaviors in such homogeneous environments will allow for the extrapolation of behaviors to heterogeneous ones (Dentz and Bolster 2010).

In order to illustrate the implications of the deposition trends outlined previously, Eq. (1) and the calculated k_d values are used to solve for and compare a travel distance (L) for each experimental condition, which serves here as a proxy for colloid mobility under the specified conditions. Similar to Jaisi et al. (2008), L is defined as the calculated distance traveled before 99% of the nanosheets have been deposited in the collector (i.e., $C/C_0 = 0.01$). This calculation results in a maximum value for L of 6.8 m in the quartz sand treatment exhibiting an ionic strength of 10 mM and an effluent pH of ~7.7. The value of L is approximately 4.5–5 times lower when the pH decreases to ~5.6 or the ionic strength increases to 50 mM, assuming that all other experimental conditions are identical. Hence, these data indicate that within the environmentally relevant electrochemical ranges of this study, pH and ionic strength impart approximately equivalent influences on the mobility of SLGO nanosheets through quartz sand. The combined influence of pH and ionic strength has been largely neglected by past studies. All values of L for the iron oxide–coated sand treatments were less than 1.0 m, illustrating the limited mobility of SLGO nanosheets in these systems.

Conclusions

This study used EPM measurements and initial deposition rate coefficients calculated from particle breakthrough curves to study the influence of environmentally relevant pH and ionic strength on the transport of SLGO nanosheets through saturated columns packed with quartz and iron oxide–coated sands. The results demonstrated that SLGO nanosheet transport was more limited in the iron oxide–coated sand treatments, relative to the quartz sand treatments, and transport was largely controlled by the relative electrochemical properties of the nanosheet and sand surfaces, as determined by both the pH and ionic strength of a given treatment. As a result, the mobility of SLGO nanosheets in each mineral-bearing system decreases with increasing ionic strength and with decreasing pH. However, several observed transport behaviors could not be explained by the respective electrochemical surfaces properties and the authors propose that nanosheet aggregation at high ionic strength and the distinctive nanosheet dimensions may also influence SLGO nanosheet transport. Collectively, these data suggest that in addition to mineral grain coatings, pH, and ionic strength, particle aspect ratio must also be considered when evaluating the mobility of engineered nanomaterials in environmental systems.

Supplemental Data

Figs. S1–S4, unprocessed breakthrough curves, and additional experimental details are available online in the ASCE Library (www.ascelibrary.org).

Acknowledgments

This research was supported, in part, by fellowships to the first author from the Arthur J. Schmitt Foundation and the National Research Council. In addition, the authors performed most experiments and analyses using instrumentation at the Center for Environmental Science and Technology (University of Notre Dame). The authors also acknowledge a substantial technical contribution by Jennifer Szymanowski (ND) and additional research guidance by Dr. Lauren Greenlee (NIST). The second author's contribution was supported by the USDOE Office of Nuclear Energy's Nuclear Energy University Programs, the U.S. National Science Foundation's Environmental Engineering Program, the donors of the ACS Petroleum Research Fund, and the University of Notre Dame Sustainable Energy Initiative. Contribution of the National Institute of Standards and Technology, an agency of the United States government; not subject to copyright in the United States. Certain commercial equipment, instruments, databases, or materials may be identified in this paper to foster understanding. Such identification does not imply recommendation or endorsement by the National Institute of Standards and Technology, nor does it imply that the materials or equipment identified are necessarily the best available for the purpose.

References

Ams, D. A., Fein, J. B., Dong, H. L., and Maurice, P. A. (2004). "Experimental measurements of the adsorption of Bacillus subtilis and Pseudomonas mendocina onto Fe-oxyhydroxide-coated and uncoated quartz grains." *Geomicrobiol. J.*, 21(8), 511–519.

Bradford, S. A., Simunek, J., Bettahar, M., Van Genuchten, M. T., and Yates, S. R. (2003). "Modeling colloid attachment, straining, and exclusion in saturated porous media." *Environ. Sci. Technol.*, 37(10), 2242–2250.

Bradford, S. A., Yates, S. R., Bettahar, M., and Simunek, J. (2002). "Physical factors affecting the transport and fate of colloids in saturated porous media." *Water Resour. Res.*, 38(12), 63/1–63/12.

Chen, C. M., et al. (2009). "Self-assembled free-standing graphite oxide membrane." *Adv. Mater.*, 21(35), NA–NA.

Chowdhury, I., Duch, M. C., Mansukhani, N. D., Hersam, M. C., and Bouchard, D. (2013). "Colloidal properties and stability of graphene oxide nanomaterials in the aquatic environment." *Environ. Sci. Technol.*, 47(12), 6288–6296.

Davis, J. A., and Leckie, J. O. (1978). "Surface ionization and complexation at oxide-water interface. 2: Surface properties of amorphous iron oxyhydroxide and adsorption of metal ions." *J. Colloid Interface Sci.*, 67(1), 90–107.

Dentz, M., and Bolster, D. (2010). "Distribution- versus correlation-induced anomalous transport in quenched random velocity fields." *Phys. Rev. Lett.*, 105(24), 244301/1–244301/4.

Dogan, A. U., Dogan, M., Onal, M., Sarikaya, Y., Aburub, A., and Wurster, D. E. (2006). "Baseline studies of the clay minerals society source clays: Specific surface area by the Brunauer Emmett Teller (BET) method." *Clays Clay Miner.*, 54(1), 62–66.

Dogan, M., Dogan, A. U., Yesilyurt, F. I., Alaygut, D., Buckner, I., and Wurster, D. E. (2007). "Baseline studies of The Clay Minerals Society special clays: Specific surface area by the Brunauer Emmett Teller (BET) method." *Clays Clay Miner.*, 55(5), 534–541.

Dreyer, D. R., Park, S., Bielawski, C. W., and Ruoff, R. S. (2010). "The chemistry of graphene oxide." *Chem. Soc. Rev.*, 39(1), 228–240.

Duster, T. A., Szymanowski, J. E. S., Na, C., Showalter, A. R., Bunker, B. A., and Fein, J. B. (2015). "Surface complexation modeling of proton and metal sorption onto graphene oxide." *Colloids Surf. A: Physicochem. Eng. Aspects*, 466, 28–39.

Feriancikova, L., and Xu, S. P. (2012). "Deposition and remobilization of graphene oxide within saturated sand packs." *J. Hazard. Mater.*, 235, 194–200.

Gao, W., Alemany, L. B., Ci, L. J., and Ajayan, P. M. (2009). "New insights into the structure and reduction of graphite oxide." *Nat. Chem.*, 1(5), 403–408.

Gao, Y., et al. (2012). "Adsorption and removal of tetracycline antibiotics from aqueous solution by graphene oxide." *J. Colloid Interface Sci.*, 368(1), 540–546.

Hartono, T., Wang, S. B., Ma, Q., and Zhu, Z. H. (2009). "Layer structured graphite oxide as a novel adsorbent for humic acid removal from aqueous solution." *J. Colloid Interface Sci.*, 333(1), 114–119.

Hummers, W. S., and Offeman, R. E. (1958). "Preparation of graphitic oxide." *J. Am. Chem. Soc.*, 80(6), 1339.

Ion, A. C., Alpatova, A., Ion, I., and Culetu, A. (2011). "Study on phenol adsorption from aqueous solutions on exfoliated graphitic nanoplatelets." *Mater. Sci. Eng. B-Adv. Funct. Solid-State Mater.*, 176(7), 588–595.

Jaisi, D. P., and Elimelech, M. (2009). "Single-walled carbon nanotubes exhibit limited transport in soil columns." *Environ. Sci. Technol.*, 43(24), 9161–9166.

Jaisi, D. P., Saleh, N. B., Blake, R. E., and Elimelech, M. (2008). "Transport of single-walled carbon nanotubes in porous media: Filtration mechanisms and reversibility." *Environ. Sci. Technol.*, 42(22), 8317–8323.

Johnson, P. R., Sun, N., and Elimelech, M. (1996). "Colloid transport in geochemically heterogeneous porous media: Modeling and measurements." *Environ. Sci. Technol.*, 30(11), 3284–3293.

Johnson, W. P., and Logan, B. E. (1996). "Enhanced transport of bacteria in porous media by sediment-phase and aqueous-phase natural organic matter." *Water Res.*, 30(4), 923–931.

Konkena, B., and Vasudevan, S. (2012). "Understanding aqueous dispersibility of graphene oxide and reduced graphene oxide through pK(a) measurements." *J. Phys. Chem. Lett.*, 3(7), 867–872.

Kretzschmar, R., Barmettler, K., Grolimund, D., Yan, Y. D., Borkovec, M., and Sticher, H. (1997). "Experimental determination of colloid deposition rates and collision efficiencies in natural porous media." *Water Resour. Res.*, 33(5), 1129–1137.

Kretzschmar, R., Borkovec, M., Grolimund, D., and Elimelech, M. (1999). "Mobile subsurface colloids and their role in contaminant transport." *Adv. Agron.*, 66, 121–193.

Lagaly, G. (2006). "Colloid clay science." *Handbook of clay science*, F. Bergaya, B. K. G. Theng, and G. Lagaly, eds., Elsevier, Amsterdam, Netherlands, 141–245.

Lanphere, J. D., Luth, C. J., and Walker, S. L. (2013). "Effects of solution chemistry on the transport of graphene oxide in saturated porous media." *Environ. Sci. Technol.*, 47(9), 4255–4261.

Lee, D. W., et al. (2010). "The structure of graphite oxide: Investigation of its surface chemical groups." *J. Phys. Chem. B*, 114(17), 5723–5728.

Lerf, A., He, H. Y., Forster, M., and Klinowski, J. (1998). "Structure of graphite oxide revisited." *J. Phys. Chem. B*, 102(23), 4477–4482.

Liu, L., et al. (2013a). "Deposition and transport of graphene oxide in saturated and unsaturated porous media." *Chem. Eng. J.*, 229, 444–449.

Liu, L., Gao, B., Wu, L., Yang, L. Y., Zhou, Z. H., and Wang, H. (2013b). "Effects of pH and surface metal oxyhydroxides on deposition and transport of carboxyl-functionalized graphene in saturated porous media." *J. Nanoparticle Res.*, 15(11), 2079.

Novoselov, K. S., et al. (2004). "Electric field effect in atomically thin carbon films." *Science*, 306(5696), 666–669.

Pagnanelli, F., Bornoroni, L., Moscardini, E., and Toro, L. (2006). "Non-electrostatic surface complexation models for protons and lead(II) sorption onto single minerals and their mixture." *Chemosphere*, 63(7), 1063–1073.

Park, S., and Ruoff, R. S. (2009). "Chemical methods for the production of graphenes." *Nat. Nano Technol.*, 4(4), 217–224.

Peigney, A., Laurent, C., Flahaut, E., Bacsa, R. R., and Rousset, A. (2001). "Specific surface area of carbon nanotubes and bundles of carbon nanotubes." *Carbon*, 39(4), 507–514.

Qi, Z., Zhang, L., and Chen, W. (2014a). "Transport of graphene oxide nanoparticles in saturated sandy soil." *Environ. Sci.: Process. Impacts*, 16(10), 2268–2277.

Qi, Z., Zhang, L., Wang, F., Hou, L., and Chen, W. (2014b). "Factors controlling transport of graphene oxide nanoparticles in saturated sand columns." *Environ. Toxicol. Chem.*, 33(5), 998–1004.

Redman, J. A., Walker, S. L., and Elimelech, M. (2004). "Bacterial adhesion and transport in porous media: Role of the secondary energy minimum." *Environ. Sci. Technol.*, 38(6), 1777–1785.

Romanchuk, A. Y., Slesarev, A. S., Kalmykov, S. N., Kosynkin, D. V., and Tour, J. M. (2013). "Graphene oxide for effective radionuclide removal." *Phys. Chem. Chem. Phys.*, 15(7), 2321–2327.

Ryan, J. N., and Elimelech, M. (1996). "Colloid mobilization and transport in groundwater." *Colloids Surf. A-Physicochem. Eng. Aspects*, 107, 1–56.

Salerno, M. B., Flamm, M., Logan, B. E., and Velegol, D. (2006). "Transport of rodlike colloids through packed beds." *Environ. Sci. Technol.*, 40(20), 6336–6340.

Sen, T. K., and Khilar, K. C. (2006). "Review on subsurface colloids and colloid-associated contaminant transport in saturated porous media." *Adv. Colloid Interface Sci.*, 119(2–3), 71–96.

Seymour, M. B., Chen, G. X., Su, C. M., and Li, Y. S. (2013). "Transport and retention of colloids in porous media: Does shape really matter?" *Environ. Sci. Technol.*, 47(15), 8391–8398.

Sitko, R., et al. (2013). "Adsorption of divalent metal ions from aqueous solutions using graphene oxide." *Dalton Trans.*, 42(16), 5682–5689.

Smith, J., et al. (2008). "Pore-scale quantification of colloid transport in saturated porous media." *Environ. Sci. Technol.*, 42(2), 517–523.

Song, L., and Elimelech, M. (1993). "Dynamics of colloid deposition in porous media—Modeling the role of retained particles." *Colloids Surf. A-Physicochem. Eng. Aspects*, 73, 49–63.

Stankovich, S., et al. (2007). "Synthesis of graphene-based nanosheets via chemical reduction of exfoliated graphite oxide." *Carbon*, 45(7), 1558–1565.

Szabo, T., Berkesi, O., Forgo, P., Josepovits, K., Sanakis, Y., Petridis, D., and Dekany, I. (2006a). "Evolution of surface functional groups in a series of progressively oxidized graphite oxides." *Chem. Mater.*, 18(11), 2740–2749.

Szabo, T., Tombacz, E., Illes, E., and Dekany, I. (2006b). "Enhanced acidity and pH-dependent surface charge characterization of successively oxidized graphite oxides." *Carbon*, 44(3), 537–545.

Tong, M. P., Ding, J. L., Shen, Y., and Zhu, P. T. (2010). "Influence of biofilm on the transport of fullerene (C-60) nanoparticles in porous media." *Water Res.*, 44(4), 1094–1103.

Tournassat, C., Neaman, A., Villieras, F., Bosbach, D., and Charlet, L. (2003). "Nanomorphology of montmorillonite particles: Estimation of the clay edge sorption site density by low-pressure gas adsorption and AFM observations." *Am. Miner.*, 88(11–12), 1989–1995.

Tufenkji, N., and Elimelech, M. (2004). "Correlation equation for predicting single-collector efficiency in physicochemical filtration in saturated porous media." *Environ. Sci. Technol.*, 38(2), 529–536.

Wang, S. B., Sun, H. Q., Ang, H. M., and Tade, M. O. (2013). "Adsorptive remediation of environmental pollutants using novel graphene-based nanomaterials." *Chem. Eng. J.*, 226, 336–347.

Weiss, T. H., Mills, A. L., Hornberger, G. M., and Herman, J. S. (1995). "Effect of bacterial-cell shape on transport of bacteria in porous media." *Environ. Sci. Technol.*, 29(7), 1737–1740.

Xu, S. P., Gao, B., and Saiers, J. E. (2006). "Straining of colloidal particles in saturated porous media." *Water Resour. Res.*, 42(12), W12S16.

Yao, K. M., Habibian, M. M., and Omelia, C. R. (1971). "Water and waste water filtration—Concepts and applications." *Environ. Sci. Technol.*, 5(11), 1105–1112.

Zhang, J. L., Yang, H. J., Shen, G. X., Cheng, P., Zhang, J. Y., and Guo, S. W. (2010). "Reduction of graphene oxide via L-ascorbic acid." *Chem. Commun.*, 46(7), 1112–1114.

Zhang, W. J., et al. (2011). "Fast and considerable adsorption of methylene blue dye onto graphene oxide." *Bull. Environ. Contam. Toxicol.*, 87(1), 86–90.

Zhao, G. X., et al. (2011a). "Removal of Pb(II) ions from aqueous solutions on few-layered graphene oxide nanosheets." *Dalton Trans.*, 40(41), 10945–10952.

Zhao, G. X., et al. (2012). "Preconcentration of U(VI) ions on few-layered graphene oxide nanosheets from aqueous solutions." *Dalton Trans.*, 41(20), 6182–6188.

Zhao, G. X., Li, J. X., Ren, X. M., Chen, C. L., and Wang, X. K. (2011c). "Few-layered graphene oxide nanosheets as superior sorbents for heavy metal ion pollution management." *Environ. Sci. Technol.*, 45(24), 10454–10462.